Article

Nanoscale Stabilization Mechanism of Sodium Sulfate Decahydrate at Polyelectrolyte Interfaces

Damilola O. Akamo, Bernadette Cladek, Monojoy Goswami, Kyle R. Gluesenkamp, Orlando Rios, and David J. Keffer*

Read Online

ACCESS | Metrics & More | Article Recommendations

ABSTRACT: Sodium sulfate decahydrate (SSD) is a low-cost phase-change material (PCM) for thermal energy storage applications that offers substantial melting enthalpy and a suitable temperature range for near-ambient applications. However, SSD's consistent phase separation with decreased melting enthalpy over repeated thermal cycles limits its application as a PCM. Sulfonated polyelectrolytes, such as dextran sulfate sodium (DSS), have shown great effectiveness in preventing phase separation in SSD. However, there is limited understanding of the stabilization mechanism of SSD by DSS at the atomic length and time scales. In this work, we investigate SSD stabilization via DSS using neutron scattering and molecular dynamics (MD) simulations. Neutron scattering and pair distribution function analysis revealed the structural evolution of the PCM samples below and above the phase change temperatures. MD simulations revealed that water from the hydrate structure migrates from the hydrate crystal to the SSD−DSS interfacial region upon melting. The water is stabilized at this interface by aggregation around the hydrophilic sulfonic acid groups attached to the backbone of the polyelectrolyte. This architecture retains water near the dehydrated sodium sulfate, preventing phase separation and, consequently, stabilizing SSD rehydration. This work provides atomistic insight into selecting and designing stable and high-performance PCMs for heating and cooling applications in building technologies.
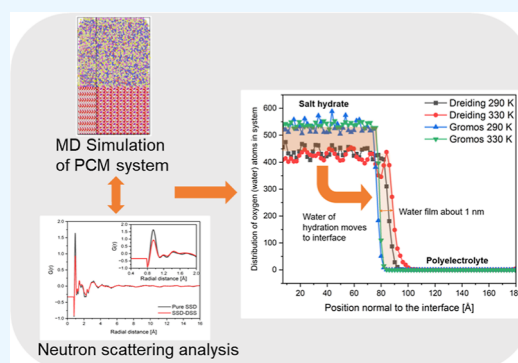
1. INTRODUCTION

Energy is a critical component of scientific innovation and economic growth, which is necessary for the improvement of societies globally.[1] As nonrenewable resources continue to be depleted and the global warming crisis worsens, the trend is shifting toward the usage of renewable energy sources.[2,3] Improvements in energy conversion and storage technologies are required to combat global energy challenges and to reduce the effect of climate change. Currently, thermal energy storage (TES) systems are proving to be among the efficient means of storing energy for use in energy systems such as heating, ventilation, and air conditioning devices,[4] solar energy storage,[5] waste heat recovery,[6] and power generation.[7] Phase-change materials (PCMs), which are a type of TES materials, have drawn the attention of many researchers due to their significant thermophysical features.[8] PCMs are particularly relevant in building applications because they can store and release energy in both sensible and latent modes. This allows them to reduce heat flow between the building and the surrounding environment thereby leading to increased energy efficiency, flexibility, and load reduction of these thermal systems.[9]

Sodium sulfate decahydrate (SSD), commonly known as Glauber's salt, is considered a viable salt hydrate PCM for building system applications due to its low cost, high melting enthalpy, and suitable melting temperature.[10,11] Several studies have reported the development and application of SSD for building technologies. Zhang et al.[12] reported the synthesis and characterization of microencapsulated SSD within a silica shell with latent heat of melting of 125.6 J/g and melting point of 33.6 °C relevant for TES. In another work, Islam and Ahmed[13] incorporated SSD in the traditional building wall to evaluate the variation in temperature inside the room with or without SSD. The study showed that SSD easily decreased the temperature fluctuation of the indoor temperature, with maximum average temperature fluctuation at 3 °C. In their investigation, Xie et al.[14] revealed a shape stabilized PCM containing SSD and sodium carbonate decahydrate in a

eutectic concentration, impregnated in expanded vermiculite. The PCM composite has a phase change temperature and latent heat of 23.98 °C and 110.3 J/g. The PCM was incorporated in insulated wallboards to evaluate indoor temperature variations. The results show that the composite was effective in regulating the indoor temperature comfortably within accepted range when compared to the baseline without PCM. Liu et al.[15] also reported the application of SSD/fly ash shape stabilized PCM mortar for building applications. The use of SSD enhanced the thermal inertia of the PCM mortar. At 15% concentration of SSD, the TES capacity of the mortar was 2.4 times that of the control samples.

In practice, the solid-to-liquid phase transition of SSD is a peritectic process upon heating to yield anhydrous sodium sulfate salt and a saturated aqueous solution of Na_2SO_4 in water.[16] The irreversible phase separation occurs if the salt settles due to gravity, forming an inhomogeneous suspension. This phase-separation behavior, which results in significant loss of latent heat during repeated melt/freeze cycles, has prohibited the widespread application of SSD as a PCM for TES applications.[17] Thus, minimizing phase separation in SSD by preventing the precipitation of anhydrous sodium sulfate salt is critical for its broad adoption as a PCM for temperature control applications. Several studies have proposed various approaches for the reduction of phase separation in SSD including gelation or thickening.[18] Gelation refers to adding a cross-linked substance (especially polymers) to the salt to form a network in which salt hydrate particles are embedded.[19] Thickening involves adding a substance to the salt hydrate that increases its viscosity and limits aggregation.[20] Numerous thickening and gelation agents, including attapulgite clay, micro/nanofibrillated cellulose, carboxymethyl cellulose, sodium alginate, hydroxyl ethyl cellulose, and polyacrylamide have been studied and examined.[21−25] However, the ionic strength of PCM salt solutions can severely impact the functionality of the thickeners.[26]

Encapsulation of the PCMs is another proposed method to prevent phase separation.[5,12,27] However, the complexity and high cost of material preparation makes the approach less desirable.[28] In a new development, Li et al.[29] reported a novel approach for the stabilization of SSD using polyelectrolyte. This was demonstrated using dextran sodium sulfate (DSS), a sulfonated polyelectrolyte that significantly improved the thermal storage capacity of the SSD over 150 cycles. Dextran sulfate sodium (DSS) is a polyelectrolyte material containing sodium sulfate groups ($-OSO_3Na$) on each repeating unit as demonstrated in Figure 1. It is hypothesized that DSS provides
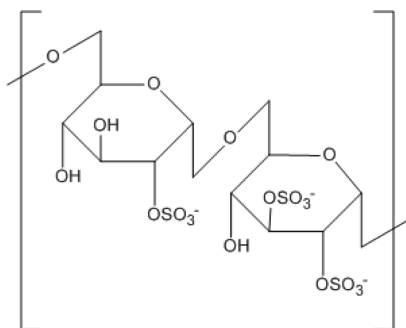
a possible electrostatic and stearic stabilization of SSD. This could be due to an electrostatic interaction between the anhydrous salt particles and the DSS polyanion, which reduces the settling rate of sodium sulfate particles and maintains their suspension in solution. Also, DSS polyanions acted as a barrier, preventing undissolved anhydrous particles from aggregating, and settling rapidly.[29] Therefore, polyelectrolyte-based materials are promising approaches for preventing phase separation in PCMs. Also, supercooling is a major phenomenon that delays the release of latent heat by SSD during solidification. This could impact the thermal storage capacity of the SSD system after successive melt/freeze cycles. To solve this problem, several nucleating agents have been proposed to trigger the crystallization of SSD during the required period. For example, sodium tetraborate decahydrate (borax) was added to SSD in varying concentrations to reduce supercooling and enhance crystallization in a timely and consistent manner.[30]

Despite extensive experimental research on SSD as PCM materials, the fundamental understanding of the effect of the polyelectrolyte additives on the properties of SSD remains unclear at the molecular level. Sankar Deepa and Tewari[31] investigated the phase transition behavior of SSD in the presence of NaCl using molecular dynamics (MD) simulations. The study found that the progressive dissociation of water molecules from the salt molecule causes a phase change from hydrated to anhydrous salts across a broad temperature range. NaCl lowers the temperature at which the phase transition occurs but increases the latent heat of melting. Results from this computational study show that when it comes to hydrated salts, hydrogen bonding capacity, and electrostatic interactions of the ionic charges are the most important variables. So far, the atomistic mechanism of polyelectrolyte stabilization of SSD has not been reported in the literature. Therefore, it is essential to acquire insight into the atomistic process behind the roles of these additives in better material design.

In the present work, we investigated the nanoscale mechanism of stabilization of SSD in the presence of DSS, using classical MD simulations and neutron scattering techniques. Particular attention is paid to the redistribution of the water of hydration below and above the melting temperature. Impact of polyelectrolyte addition on the structure and dynamics of SSD is investigated. This work is significant because it serves as a guide in the design and characterization of other relevant polyelectrolytes with SSD for various target applications.

2. METHODS

2.1. Experimental Setup. *2.1.1. Materials Preparation.* As the hydrogen atom has a highly incoherent neutron scattering cross section, it was required to utilize the perdeuterated analogous salt hydrate to improve the signal-to-noise ratio of our diffraction measurements. Hence, anhydrous salt, Na_2SO_4 (Sigma-Aldrich, ACS reagent, ≥99%), deuterium oxide (D_2O) (Sigma-Aldrich, 99 atom % D), and dextran sulfate sodium polyelectrolyte (DSS) (Sigma-Aldrich, $M_r \sim 500,000$) were used to prepare the perdeuterated salt hydrate PCM. Na_2SO_4 and D_2O were mixed in appropriate weight ratio and stirred at 60 °C for 2 h to obtain the perdeuterated salt hydrate. For the SSD−DSS mixture, 5 wt % DSS was added to the perdeuterated SSD and mixed using the same temperature and time as the perdeuterated salt hydrate.
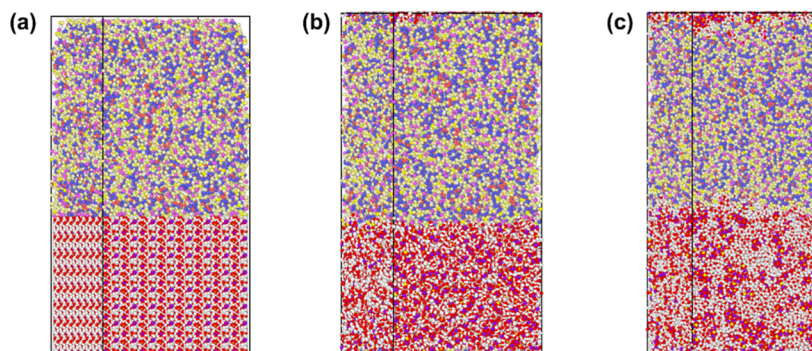

Figure 1. Molecular structure of dextran sulfate sodium polyelectrolyte.

Figure 2. Simulation box snapshot (a) initial system with perfect crystal of SSD (bottom), (b) system at 290 K using the GROMOS potential showing some degree of crystallinity, and (c) system at 330 K using the Dreiding potential with loss of crystal structure in SSD. Color legend: (SSD—yellow: S, red: O, purple: Na, white: H; DSS—blue: H, red: carbon, light yellow: O, white: H, deep yellow: S, pink: Na).

2.1.2. Materials Characterization. The phase change temperature of the SSD was evaluated by subjecting the samples to a 50 mL/min nitrogen purge in a differential scanning calorimeter (DSC 2500, TA Instruments). Hermetically sealed aluminum DSC pans were used to conduct heat cycling between 233 and 320 K on the sample weighing 10−20 mg. The phase change temperature of the PCM samples was determined by using the heating scan.

To determine the nanoscale structure of the materials, two perdeuterated samples of based on pure SSD, and a mixture of SSD with DSS were analyzed using the nanoscale-ordered materials diffractometer (NOMAD) beamline at the Spallation Neutron Source at Oak Ridge National Laboratory to measure pair distribution functions (PDFs).[32] Neutron time-of-flight diffraction offers higher-resolution PDFs due to the greater Q range available, and neutrons are more sensitive to the light elements than X-rays.[33] Around 1.5 g of the samples were loaded in a 6-mm V sample canister. As a final step before loading the sample canister, the samples were melted. Diamond was utilized to calibrate NOMAD's detectors, while silicon was employed to obtain instrumental parameters. The scattering from the sample was normalized using a solid vanadium rod, and the background for an empty 6 mm V sample canister was subtracted to get $S(Q)$. Each sample was first cooled to room temperature and then ramped from 290 to 330 K during which neutron data are collected. Neutrons scans were collected for 30 min at each temperature between 290 and 330 K. The PDF data was converted from reciprocal to real space using the StoG feature $[S(q)$ to $G(r)]$ included in the RMCProfile software.[34]

2.2. MD Simulation. Classical MD simulations were performed using the LAMMPS software.[35] These simulations require (i) stable initial configurations of all atoms and (ii) inter- and intraatomic interaction potentials, known as forcefield, which describe the potential energy and forces between all types of atoms included in the simulation. The initial structure of DSS was obtained from the literature[36] consisting of 12 monomers in each chain that was relaxed using Avogadro.[37] The degree of sulfonation was introduced by adding two sulfonic acid groups per monomer. The polyelectrolyte melt was composed of 175 short 12-mer DSS chains, resulting in 61,425 atoms. The melt was initialized with random orientations of DSS and equilibrated for 500 ps at 1000 K.

The crystal structure of SSD was determined using the crystallographic datafile obtained from the work of Kamburov

et al.[30,38] The unit cell was extended by 8 × 8 × 8 units, generating 75,776 atoms. The SSD was separately equilibrated in the NpT ensemble. Finally, the DSS molecules were placed adjacent to the SSD crystal in a monoclinic simulation box, based on the initial monoclinic crystal structure of SSD, extended in the [001] dimension to accommodate the melt. The combined system contains 137,201 atoms, as shown in Figure 2a.

In a classical MD simulation, the interaction potential is an essential input. The choice of interaction potential depends upon the questions being asked and ultimately defines the physics contained within the model. For this system, a flexible model of the polymer was introduced, which includes all intramolecular degrees of freedom, including bond stretching, bond angles, dihedral torsion, as well as nonbonded interactions. The interatomic forces consisted of Lennard-Jones and Coulombic terms. For the DSS polyelectrolyte, the Dreiding potential was used. The Dreiding force-field is a generic force field that can provide an accurate forecast of the structures and dynamics of organic, biological, and main-group inorganic compounds.[39]

For the interatomic potential of the SSD hydrate, simulations were performed with two different interaction potentials. First, the Dreiding potential was again used for SSD. Second, the GROMOS 54a7-FF potential for sodium and sulfate values[40] and an SPC/E model for the water molecules[41] were used. Both potentials employed a short-range cutoff of 12 Å and used the Ewald summation to evaluate long-range electrostatic interactions in reciprocal space. Neither the Dreiding nor the GROMOS potential were parametrized to capture the precise melt temperature of SSD. Therefore, simulations using both potentials turned out to be illustrative.

The two-phase simulation box for SSD−DSS simulations used periodic boundary conditions in all directions, creating an infinite surface. Equilibration of the two-phase system was performed in the isobaric−isothermal (NpT) ensemble at 1 atm to obtain the correct system density, using a Nosé− Hoover thermostat and barostat.[42,43] The time step for the MD simulation was set at 1 fs. The thermostat and barostat damping parameters were 100 and 1000 fs, respectively. Equilibration of the two-phase system lasted 1.0 ns. Data production was performed in the canonical (NVT) ensemble and lasted for 0.5 ns. The results of four simulations are reported, which include two temperatures, 290 K (below melt temperature of 304.5 K) and 330 K (above melt temperature), using both the Dreiding and GROMOS potentials. Snapshots
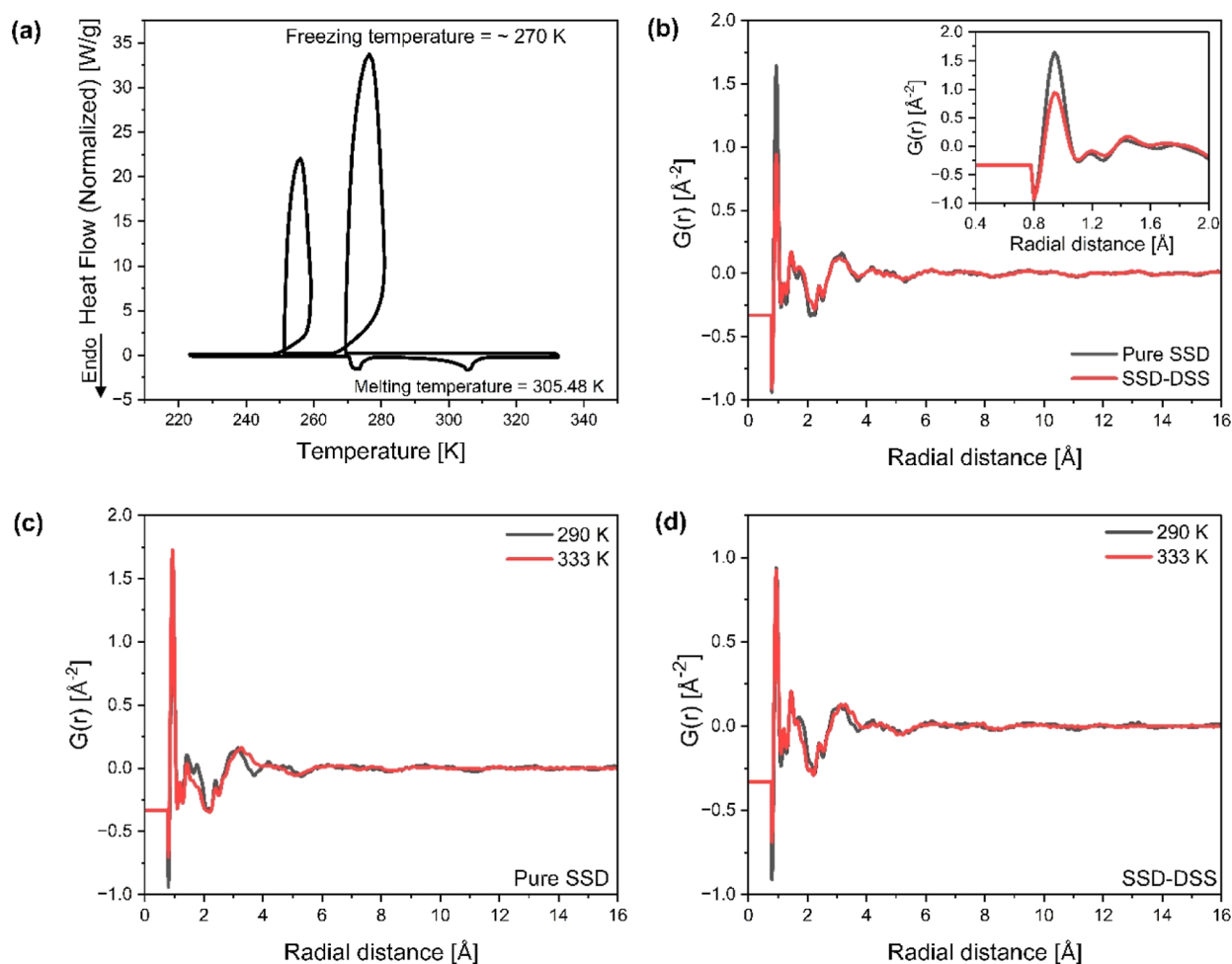
Figure 3. (a) DSC plot showing the melting and freezing temperatures of SSD. Endothermic melting peak is pointing downward while exothermic freezing peak is pointing upward. (b) Neutron PDF data for SSD and SSD−DSS mixture obtained from NOMAD at 290 K. (c) PDF data for SSD at 290 and 333 K (d) PDF data for SSD−DSS mixture at 290 and 333 K.

of the equilibrated system at 290 and 330 K are shown in Figure 2b,c respectively.

3. RESULTS AND DISCUSSIONS

3.1. Thermal and Structural Properties of SSD and SSD−DSS Obtained from Experiment. The melting and freezing data of pure SSD from the DSC experiment are shown in Figure 3a. The melting result showed that SSD undergoes a solid−liquid phase transition at 305.48 K. This is consistent with the data reported in the literature.[30,31] The freezing data showed that SSD crystallized at a temperature of 270 K, which showed that the salt hydrate has a high degree of supercooling. It should be noted that the recalescence in the freezing peak is due to the evolution of the latent heat of freezing during the partial crystallization of water. In our previous study, it was reported that the SSD−DSS PCM system is ~307 K.[16] This is very similar to the melting point of pure SSD, which means the addition of the DSS polyelectrolyte did not change the melting point of the pure SSD substantially. However, the phase transition temperature provides a guide for the temperature range selection considered for the experimental neutron scattering experiment and the MD simulations (290 K, below the melting point and 330 K, above the melting point). The experimental neutron PDF data for SSD and the SSD−DSS mixture are shown in Figure 3b. The PDF data

correlates relative atomic positions by assessing the probability of one atom's position with respect to neighboring atoms.[44]

Each peak in the PDF data represents the atomic distance between the reference atom and the other neighboring atoms. Because of this capability, the PDF could be used as a standard for determining the local atomic structure and configuration of materials.[45,46] The total PDF, $G(r)$, which is experimentally measured, is defined as[47]

$$G(r) = \sum_A \sum_B c_A c_B \overline{b_A}\, \overline{b_B}[g_{AB}(r) - 1] \tag{1}$$

where $\overline{b_A}$ and $\overline{b_B}$ are the average scattering power of atomic species A and B respectively, c_A and c_B are the atomic concentration of the species, and $g_{AB}(r)$ is the correlation between a pair of atoms of types A and B expressed as

$$g_{AB}(r) = \frac{1}{4\pi N_A r^2 \rho_B}\sum_{i=1}^{N_A}\sum_{j=1}^{N_B} \delta(r - r_{ij}) \tag{2}$$

where N_A is the total number of atoms of type A, ρ_B is the average number density of atom of type B, and r_{ij} is the distance between atoms i and j. The Dirac delta function, denoted as $\delta(r - r_{ij})$, has a value of unity when $r - r_{ij}$ and zero otherwise. The atomic correlations for any arbitrary AB atom

type pair, $g_{AB}(r)$, are only available from simulation. Experimentally, only a total PDF, $G(r)$, is accessible.

In Figure 3b, the total PDF data for the pure SSD hydrate and the SSD−DSS hydrate-polyelectrolyte mixture are compared at 290 K. The purpose of this comparison is to demonstrate that the presence of DSS does not alter the structure of SSD at 290 K. The PDF data of the pure SSD and SSD−DSS mixture samples are very similar, which is expected since the SSD−DSS mixture contained 95 wt % SSD. The peak at 0.96 Å as shown by the inset in Figure 3b is correlated to the deuterium and oxygen (O−H) bond distance in deuterated water. This peak intensity is reduced in the sample with DSS due to the presence of hydrogen in DSS which has a negative scattering length and reduces the scattering intensity of the bond at 0.96 Å. The peak at 1.57 Å is attributed to the sulfur−oxygen bond in the sulfate anion, and the peak at 2.43 Å is correlated to the oxygen−oxygen distance in the sulfate anion.

In Figure 3c, the total PDF data for the pure SSD hydrate at 290 and 333 K is compared. Peaks that correspond to covalent bonds remain at both temperatures, since the phase change does not correspond to the breakage of any chemical bonds. However, at the higher temperature, we observe significant loss of structure. From the combined DSC and PDF data, the loss of structure can be attributed to the loss of water coordination in the crystalline hydrate. In Figure 3d, the PDF data for the SSD−DSS mixture at 290 and 333 K is compared. The primary purpose of showing the scattering data for the mixture is to demonstrate the similarity with that of the pure system. The presence of polyelectrolyte has a nominal impact on the structure of the hydrate both below and above the melting temperature.

3.2. Atomic Structure of SSD from MD Simulation. To understand the structural properties of the salt hydrate-polyelectrolyte system, the PDFs were obtained and processed from the MD simulations. First, we reproduced the total RDFs of the system at 290 and 330 K as reported in Figure 4. The peaks observed in the total RDFs of the experiment for the SSD−DSS mixture around 1, 1.65, and 3.5 Å (Figure 3) are also noticeable in the total RDF of the simulations. However, the peak intensity was more pronounced at 290 K compared to the 330 K, due to the loss in crystallinity with increase in temperature. Since the total RDF does not provide insight into
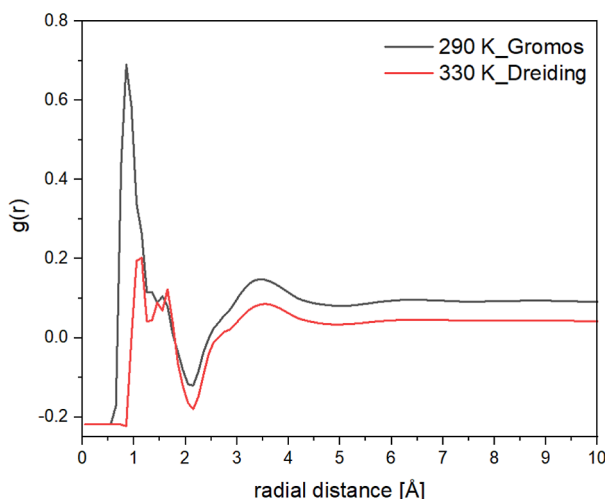

Figure 4. PDF data for SSD−DSS mixture obtained from MD simulations for Dreiding at 290 K, and GROMOS at 330 K.

the contributions of each atomic species in the system, we decomposed the RDFs and compared the atomic structure of SSD salt hydrate at 290 and 330 K based on the Dreiding potential and the GROMOS potential as shown in Figure 5. To confirm the level of crystallinity of the salt hydrate at 290 K, the sulfur−sulfur atomic distances were plotted, as shown in Figure 5a. To be clear, the only sulfur included in this calculation was those of the hydrate, as designated by the symbol, S_h. Also, note that the PDFs generated from MD simulation are reported to longer distances than was done for the experimental neutron data, because from the atom specific contributions to the PDF, certain features are evident that are washed out or harder to identify in the total PDF of neutron experiments. The $S_h−S_h$ PDF data based on the GROMOS potential showed notable sharp peaks, with a notable peak at 9.55 Å, corresponding to the spacing of adjacent S atoms in the SSD hydrate unit cell.

However, the $S_h−S_h$ PDF based on the Dreiding potential shows much less crystallinity. As noted above, neither interaction potential was developed to reproduce the SSD crystal structure or its melt temperature. From these data, it is evident that the GROMOS potential does a better job of retaining the SSD crystal structure at 290 K than the Dreiding potential. In Figure 5b, the PDF of oxygen−oxygen atomic distances are shown. The only oxygen atoms used in this calculation are those in the water of hydrates and are designated, O_h. Oxygen atoms in the sulfonate group or in the polyelectrolyte are not included in Figure 5b. The $O_h−O_h$ PDF generated from simulations using the GROMOS potential clearly shows more features of crystallinity, particularly the shoulders on both sides of the first peak. The $O_h−O_h$ PDF generated from simulations using the Dreiding potential at 290 K shows a much more liquid-like structure.

In Figure 5c, the $S_h−S_h$ PDFs for simulation at 330 K for both potentials are shown. By comparing the $S_h−S_h$ PDFs for the GROMOS potential at 290 (Figure 5a) and 330 K (Figure 5c), one can see that the crystallite has lost much of its structure but has not completed the phase transformation. On the other hand, the $S_h−S_h$ PDF for the Dreiding potential shows an almost completely liquid-like state at 330 K. The $O_h−O_h$ PDFs at 330 K, shown in Figure 5d corroborate this observation.

Based on these observations, we conclude that the GROMOS potential is better at capturing the SSD hydrate structure at 290 K while the Dreiding potential does a better job of describing the disordered SSD liquid at 330 K. Neither potential captures the 304.5 K phase transition temperature perfectly. In classical MD, simulations reflect the goodness of the interaction potential. In this case, we are compelled to use two different interaction potentials to describe the SSD phases below (GROMOS) and above (Dreiding) the melt temperature. For the practicing eye, accustomed to looking at PDFs, one may note that these PDFs do not approach the asymptote of unity at long distances. The difference in asymptote arises because the simulation system is a two-phase system and the hydrate occupies only approximately half of the simulation volume, which skews the normalizing density in eq 2.

3.3. Role of Dextran Sulfate Sodium. To understand the stabilization mechanism of DSS on SSD, it is important to investigate the structural properties at the interface between SSD and DSS. To describe these interactions, the PDFs were generated involving the sulfur atom of the sulfonic acid group on the polyelectrolyte, designated S_p, and oxygen atoms in the
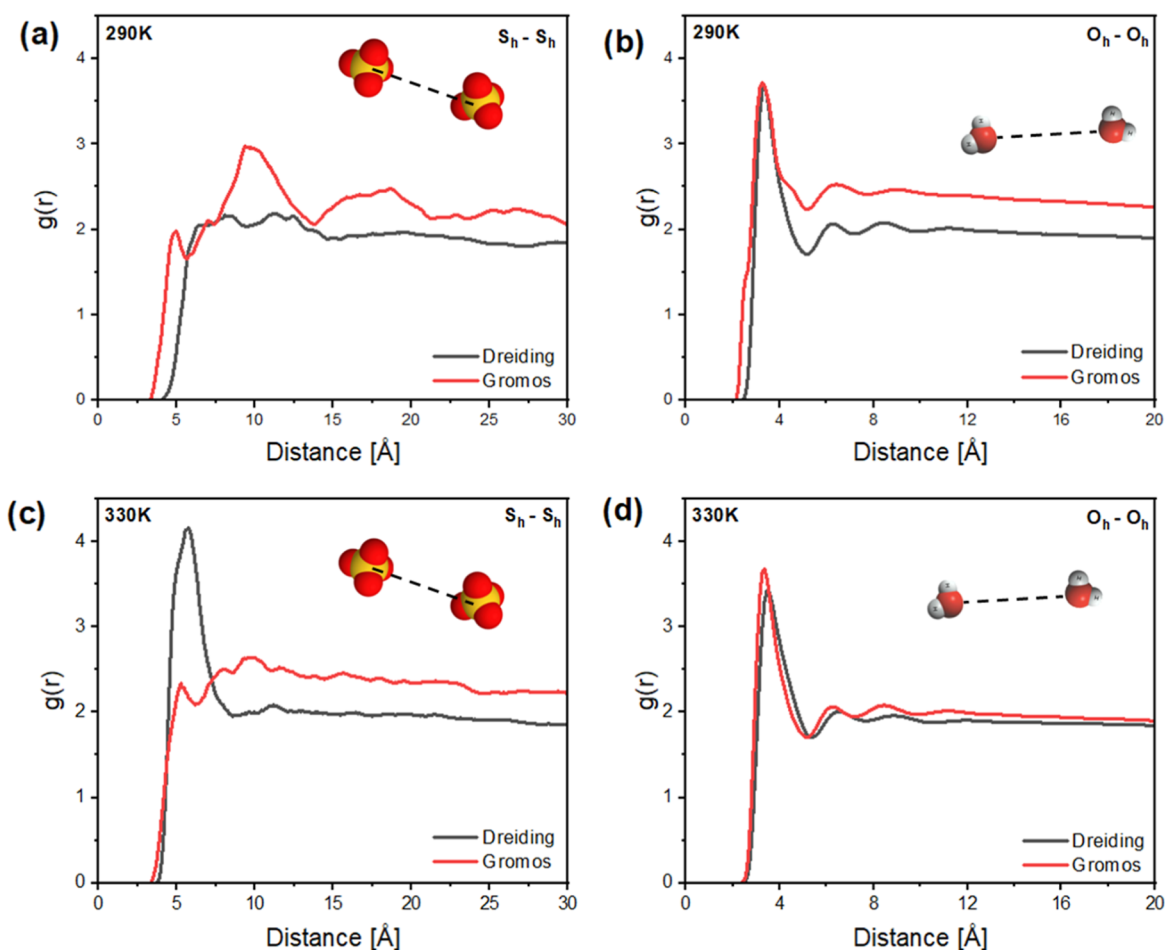
Figure 5. Simulated PDF data for SSD using two different potentials. (a) $S_h–S_h$ PDF at 290 K, (b) $O_h–O_h$ PDF at 290 K; (c) $S_h–S_h$ PDF at 330 K; (d) $O_h–O_h$ PDF at 330 K. The symbol, S_h, corresponds to sulfur atoms in the hydrate. The symbol, O_h, corresponds to oxygen atoms in the water of hydration.

backbone of the polyelectrolyte, designated as O_p. The $S_p–O_h$ PDF characterizes the aggregation of the water of hydration, O_h, with the polyelectrolyte sulfonic acid group. The $O_p–O_h$ PDF characterizes the potential aggregation of the water of hydration, namely, O_h, with the polyelectrolyte backbone. The $S_p–S_h$ PDF characterizes the aggregation of the hydrate sulfur, S_h, with the polyelectrolyte sulfonic acid group, S_p. These three PDFs are shown in Figure 6 for simulations at both 290 and 350 K, using both the GROMOS and Dreiding potentials. In these figures the GROMOS simulation at 290 K represents the best model of SSD in the solid hydrate phase and the Dreiding simulation at 330 K represents the best model of liquid SSD.

In Figure 6a,d, the $S_p–O_h$ PDF is shown at 290 and 330 K respectively. Two consequences of these PDFs are immediately clear. First, at both temperatures, the more liquid-like state described by the Dreiding potential predicts significantly more water aggregation around the sulfonic acid group of the polyelectrolyte. Second, for both potentials, as the temperature increases, the amount of water around the sulfonic acid group increases. A more detailed inspection shows that at 290 K, the water molecules cluster around sulfonic acid group at 3.25 Å. The second hydration layer was around 6.25 Å at 290 K, as revealed by the Dreiding potential; some offset of 3.65 Å, and 6.95 Å was observed with the GROMOS potential. Interestingly at 330 K, the PDF peak intensity increased as shown in Figure 6d.

From the discussion of the PDF, it can be seen that the water molecules of the dissolved hydrate prefer to remain near the interface between the SSD and DSS instead of diffusing deep inside the polyelectrolyte. The observation of localized aqueous domains centered on sulfonic acid groups tethered to polymer backbones is typically observed in the water distribution around charged polymers, such as polyelectrolytes. For example, the atomic-scale distribution of water in Nafion fuel cell membranes, is described by aggregation of water molecules around the sulfonic acid groups tethered by sidechains to the polymer backbone as has been observed by Cui et al.[48]

In Figure 6b,e, the $O_p–O_h$ PDF is shown at 290 and 330 K, respectively. As was the case for the sulfonic acid group, the Dreiding potential shows more water around the O in the polyelectrolyte backbone compared to the GROMOS potential, and the amount of water increases with temperature, as the hydrate becomes less stable. However, the extent of increase in water with temperature is less than that observed around the sulfonic acid group, indicating that the highly polar acid groups provide better electrostatic anchors around which water preferentially aggregates. In Figure 6c,f, the S_pS_h PDF is shown at 290 and 330 K, respectively. Interestingly, we do not observe aggregation of sulfur from the hydrate sulfate and the polyelectrolyte sulfonic acid group with increasing temperature. Rather, the degree of association diminishes with the
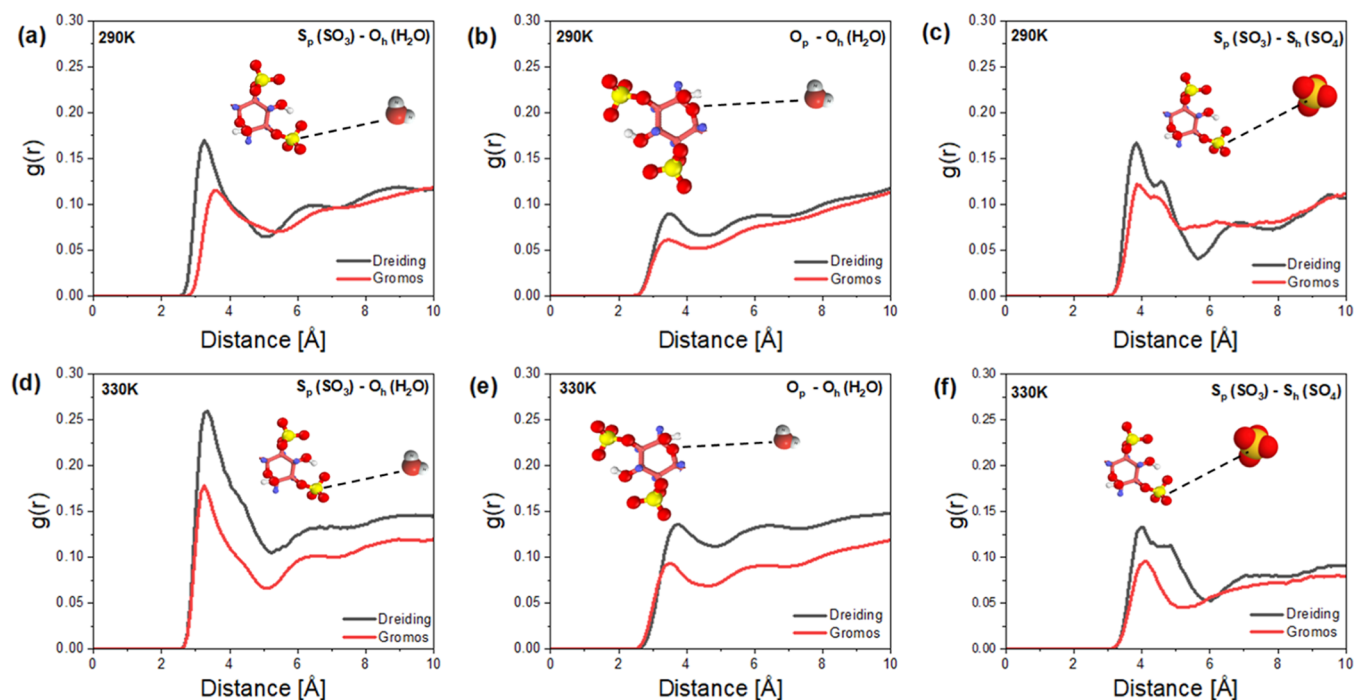
Figure 6. PDF data illustrating the interaction of atoms in the polyelectrolyte and salt hydrate (a) S_p–O_h at 290 K, (b) O_p–O_h at 290 K, (c) S_p–S_h at 290 K, (d) S_p–O_h at 330 K, (e) O_p–O_h at 330 K, (f) S_p–S_h at 330 K. Subscript "h" represents the atoms in the salt hydrate while p represents the atoms in the polyelectrolytes.

temperature. It appears that the redistribution of the water from hydration forms a thin film between the sulfate anions and the sulfonic acid groups.

It is important to state the correlation mechanism between the nanoscale and the macroscopic performance of the PCM system. Specifically, the concentration ratio of the polyelectrolyte and salt hydrate in the MD simulation system on the nanoscale is approximately 50:50. With adequate composition of DSS in the PCM composite, phase separation was mitigated by the polyelectrolyte, which sustains hydrated water in the aqueous domain. However, Li et al.[29] showed that the presence of 5 wt % DSS in the PCM composite weighed ∼ 20 g was not able to fully mitigate phase separation in SSD after a long duration; this could be because the polyelectrolyte was saturated with the water of hydration with inadequate electrostatic effect to keep them in domain. Hence, this interpretation reconciles the observations from simulation and experiment.

3.4. Interfacial Thickness and Mobility Characterization. To characterize the structure at the interface between SSD and DSS, relevant interfacial parameters were calculated using the distribution of the oxygen atom in the hydrating water, O_h, along the axis normal to the plane of the interface in simulation. The resulting water density profile is shown in Figure 7. The most immediate observation from this plot is the significant difference in the amount of water in the more solid-like SSD (GROMOS) compared to the more liquid-like SSD (Dreiding). The solid SSD has a higher plateau of water density. In the liquid SSD, water has clearly moved to the interface between SSD and DSS. In both cases, the ability for water to penetrate into the DSS is very limited. The difference in the water density as a function of temperature is slight, but the Dreiding potential in particular shows that in the liquid state, more water moves to the interface with increasing temperature. This observation is consistent with the observa-

tion of hydrated water forming a local film between the SSD and DSS, which is stabilized by aggregation around the sulfonic acid groups present at the interface.

The interfacial thickness can be determined by fitting the density profile to a functional form of the hyperbolic tangent[49]

$$D_i(z) = D_0\left[1 - \tanh\left(\frac{2(z - z_0)}{d}\right)\right] \quad (3)$$

where $D_i(z)$ is the density distribution (count) based on the position normal to the interface, D_0 is the parameter related to the plateau distribution density (count), z_0 is the position of the Gibbs dividing surface (Å), and d is the interfacial thickness (Å). The interfacial fitting results are listed in Table 1. The parameter related to the interfacial thickness d showed a higher value in all the cases for the liquid-like state compared to the solid-like state. The thickness of the water film can be estimated by examining the change in the position of the Gibbs dividing surface between the solid-like and liquid-like simulations. This thickness is nominally 1 nm.

The motion of the different atoms can be explored by calculating the mean square displacement (MSD). The MSD is relevant in the determination of the transport and diffusion characteristics of materials system[50,51] and is given by

$$\text{MSD}_A(\tau) = \langle|\vec{r_i}(t + \tau) - \vec{r_i}(t)|^2\rangle \quad (4)$$

The MSD of atoms of type A is an autocorrelation function of the elapsed time, τ, and is based on the position of all atoms of type A. The angled brackets in eq 3 represent an ensemble average of all atoms, i, of type A and all time origins, t.

The MSDs of water molecules using the two interatomic potentials at 290 and 330 K are plotted in Figure 8. We observed that the MSD increases with temperature. However, the magnitude of the highest MSD (dried at 330 K) is less than 1.5 Å². Based on the investigated time, the water molecules on
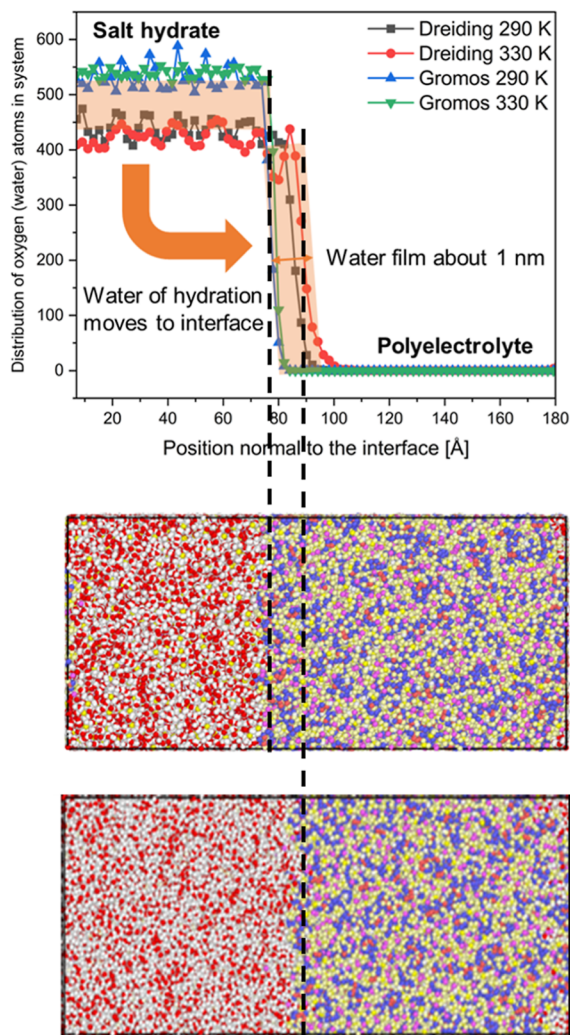
Figure 7. Distribution of oxygen atoms (water) along position normal to the interface. Water of hydration migrates toward the DSS polyelectrolyte and forms an aqueous film of 1 nm. The middle snapshot is from a simulation using the GROMOS potential at 290 K and the bottom snapshot is from a simulation using the Dreiding potential at 330 K.

Table 1. Interfacial Parameters for the Oxygen Atoms in SSD

force field	temperature (K)	D_0 (count)	z_0 (Å)	d (Å)
Dreiding	290	218.47	85.63	6.64
	330	208.67	89.43	7.14
GROMOS	290	263.72	77.23	4.70
	330	261.90	78.94	3.21

average have not moved any significant distance. This observation is consistent with a simulation where the water molecules do not diffuse deep into the surrounding polyelectrolyte. It is a result consistent with the density profile shown above. Of note, the MSD is traditionally used to generate self-diffusivities through the Einstein relation. In this simulation, the Einstein relation is not used to calculate diffusion coefficients because it is valid only in a long-time limit, and the very small values of the MSD reported here do not correspond to this limit.

3.5. Energetics. In an effort to understand the thermodynamics of the phase change, we decomposed the nonbonded
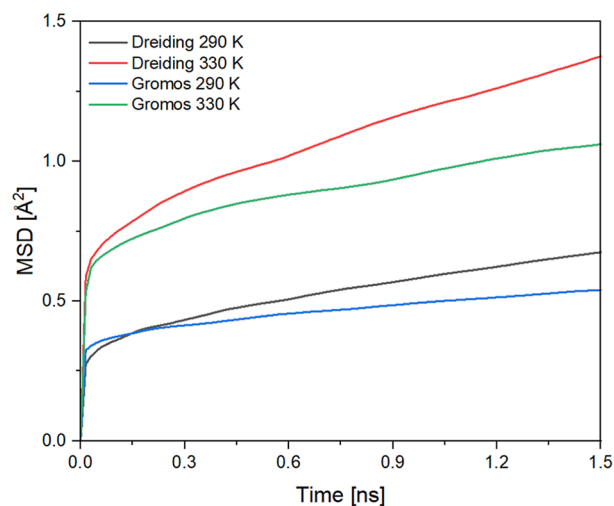

Figure 8. Comparison of MSD of water molecules in the system at 290 and 330 K for both the Dreiding and GROMOS interaction potentials.

contributions (i.e., Lennard Jones and Coulombic terms) of the potential energy into three parts: interactions between atoms in the hydrate with other atoms in the hydrate (H–H), atoms in the hydrate with atoms in the polyelectrolyte (H–P) and atoms in the polyelectrolyte with other atoms in the polyelectrolyte (P–P). In Table 2, we report the difference in

Table 2. Difference in Interaction Energy between the Components at 290 and 330 K

interaction/phase	Dreiding [kCal/mol]	GROMOS [kCal/mol]
hydrate–polymer	−16,300 ± 500	3700 ± 100
polymer–polymer	7000 ± 900	16,000 ± 800
hydrate–hydrate	−7000 ± 500	1000 ± 800
total potential energy	−7000 ± 400	20,000 ± 800
phase at 290 K	liquid with some short-range ordering	solid
phase at 330 K	liquid	disordered solid

each of these contributions between the simulations at 330 K and those at 290 K. Note that the sum of the three components does not sum to the total because the three components included only nonbonded interactions, whereas the total includes both nonbonded and bonded interactions.

In Table 2, we observe in the simulations with the GROMOS potential that all three nonbonded components (H–H, H–P, P–P) of the potential energy change from 290 to 330 K as well as the total are positive. This is to be expected; as the temperature increases, the greater kinetic energy results in atoms exploring energetically less favorable phase space. Furthermore, with the GROMOS potential, we observe a partial melting from 290 to 330 K. The exothermic process of melting also contributes to potential energy increase. In the simulations with the GROMOS potential, the greatest contribution to the change in potential is due to the polyelectrolyte interacting with itself. PDFs of the S_p–S_p, S_p–Na_p^+ and Na_p^+–Na_p^+ (not shown) reveal an increase in aggregation of all of these charged groups that is energetically unfavorable.

With the Dreiding potential, the changes in the potential energy tell a different story, describing a transition from a constrained intermediate state to a liquid state. In the simulations using the Dreiding potential, there is a net reduction in the total potential energy driven by stabilization in the hydrate–polyelectrolyte interaction. This involves the rearrangement and aggregation of water around sulfonic acid groups, leading to the stabilization of the liquid system. This phenomenon is also observed in the PDFs of Figure 6 and the density profile in Figure 7. In these more liquid-like simulations, the water of hydration is able to aggregate around the sulfonic acid groups and form a stable local aqueous film at the interface. While the P–P energy change remains exothermic, the H–H component is endothermic, and corresponds to a partial rearrangement from the hydrate to a more stable Na_2SO_4 salt-like structure as seen by the presence of a peak in the S_h–S_h PDF (Figure 5a,c).

4. CONCLUSIONS

In this work, it was discovered that the addition of polyelectrolyte dextran sulfate sodium to SSD keeps the water of hydration in close atomic proximity to the salt, thereby preventing the longstanding issue of phase segregation in SSD. The water of hydration migrates to the interface between the hydrate and polyelectrolyte, aggregating around the sulfonic acid groups of the polyelectrolyte. The acid groups are spaced sufficiently close together so that a thin film of water forms. This interfacial film is sufficiently stable so that the water is relatively immobile and does not penetrate further into the polyelectrolyte, at least on the time scale of these simulations. The thermodynamic driving force for this stabilization is found to be the interaction between the water of hydration and the polyelectrolyte.

This insight was made possible through the combination of total neutron scattering and a MD simulation. Total neutron scattering confirmed that the presence of DSS did not alter the structural transformation. MD simulation provided a decomposition of the PDF, density profiles, MSDs, and potential energies providing atomic scale insights into the salt hydrate–polyelectrolyte composites. Simulations were performed with two interaction potentials, Dreiding and GROMOS to better describe both phases of SSD. From these fundamental observations of the atomic mechanism of the stabilization of SSD by DSS, this research can influence the selection and design of novel PCM composites with improved thermal characteristics for long-term use in buildings and other commercial heating and cooling applications.

■ AUTHOR INFORMATION

Corresponding Author

David J. Keffer − *Materials Science and Engineering Department, University of Tennessee, Knoxville, Tennessee 37996, United States;* ⓘ orcid.org/0000-0002-6246-0286; Email: dkeffer@utk.edu

Authors

Damilola O. Akamo − *The Bredesen Center for Interdisciplinary Research and Graduate Education, University of Tennessee, Knoxville, Tennessee 37996, United States; Buildings and Transportation Sciences Division, Oak Ridge National Laboratory, Oak Ridge, Tennessee 37830, United States*

Bernadette Cladek − *Materials Science and Engineering Department, University of Tennessee, Knoxville, Tennessee 37996, United States;* ⓘ orcid.org/0000-0001-8538-6827

Monojoy Goswami − *Chemical Sciences Division, Oak Ridge National Laboratory, Oak Ridge, Tennessee 37830, United States;* ⓘ orcid.org/0000-0002-4473-4888

Kyle R. Gluesenkamp − *Buildings and Transportation Sciences Division, Oak Ridge National Laboratory, Oak Ridge, Tennessee 37830, United States*

Orlando Rios − *Materials Science and Engineering Department, University of Tennessee, Knoxville, Tennessee 37996, United States*

Complete contact information is available at:
https://pubs.acs.org/10.1021/acsomega.3c09796

Notes

The authors declare no competing financial interest.

■ REFERENCES

(1) Fais, B.; Sabio, N.; Strachan, N. The critical role of the industrial sector in reaching long-term emission reduction, energy efficiency and renewable targets. *Appl. Energy* **2016**, *162*, 699−712.

(2) Chen, S.; Liu, P.; Li, Z. Low carbon transition pathway of power sector with high penetration of renewable energy. *Renewable Sustainable Energy Rev.* **2020**, *130*, 109985.

(3) Pereira da Cunha, J.; Eames, P. Thermal energy storage for low and medium temperature applications using phase change materials − A review. *Appl. Energy* **2016**, *177*, 227−238.

(4) Zeinelabdein, R.; Omer, S.; Gan, G. Critical review of latent heat storage systems for free cooling in buildings. *Renewable Sustainable Energy Rev.* **2018**, *82*, 2843−2868.

(5) Raul, A.; Jain, M.; Gaikwad, S.; Saha, S. K. Modelling and experimental study of latent heat thermal energy storage with encapsulated PCMs for solar thermal applications. *Appl. Therm. Eng.* **2018**, *143*, 415−428.

(6) Xu, H.; Romagnoli, A.; Sze, J. Y.; Py, X. Application of material assessment methodology in latent heat thermal energy storage for waste heat recovery. *Appl. Energy* **2017**, *187*, 281−290.

(7) Zhao, C. Y.; Ji, Y.; Xu, Z. Investigation of the $Ca(NO_3)_2$-$NaNO_3$ mixture for latent heat storage. *Sol. Energy Mater. Sol. Cells* **2015**, *140*, 281−288.

(8) Khan, Z.; Khan, Z.; Ghafoor, A. A review of performance enhancement of PCM based latent heat storage system within the context of materials, thermal stability and compatibility. *Energy Convers. Manage.* **2016**, *115*, 132−158.

(9) Kumar, N.; Hirschey, J.; LaClair, T. J.; Gluesenkamp, K. R.; Graham, S. Review of stability and thermal conductivity enhancements for salt hydrates. *J. Energy Storage* **2019**, *24*, 100794.

(10) Marks, S. An investigation of the thermal energy storage capacity of Glauber's salt with respect to thermal cycling. *Sol. Energy* **1980**, 25 (3), 255−258.

(11) Marks, S. B. The effect of crystal size on the thermal energy storage capacity of thickened Glauber's Salt. *Sol. Energy* **1983**, 30 (1), 45−49.

(12) Zhang, Z.; Lian, Y.; Xu, X.; Xu, X.; Xu, X.; Gu, M.; Gu, M. Synthesis and characterization of microencapsulated sodium sulfate decahydrate as phase change energy storage materials. *Appl. Energy* **2019**, 255, 113830.

(13) Islam, M. N.; Ahmed, D. H. Delaying the temperature fluctuations through PCM integrated building walls—Room conditions, PCM placement, and temperature of the heat sources. *Energy Storage* **2021**, 3 (5), No. e245.

(14) Xie, N.; Luo, J.; Li, Z.; Huang, Z.; Gao, X.; Fang, Y.; Zhang, Z. Salt hydrate/expanded vermiculite composite as a form-stable phase change material for building energy storage. *Sol. Energy Mater. Sol. Cells* **2019**, 189, 33−42.

(15) Liu, L.; Lu, G.; Qiu, G.; Yue, C.; Guo, M.; Ji, R.; Zhang, M. Characterization of novel shape-stabilized phase change material mortar: Portland cement containing $Na_2SO_4 \cdot 10H_2O$ and fly ash for energy-efficient building. *Int. J. Energy Res.* **2019**, 43 (11), 5812−5823.

(16) Akamo, D. O.; Kumar, N.; Li, Y.; Pekol, C.; Li, K.; Goswami, M.; Hirschey, J.; LaClair, T. J.; Keffer, D. J.; Rios, O.; et al. Stabilization of low-cost phase change materials for thermal energy storage applications. *iScience* **2023**, 26 (7), 107175.

(17) Dong, X.; Mao, J.; Geng, S.; Li, Y.; Hou, P.; Lian, H. Study on performance optimization of sodium sulfate decahydrate phase change energy storage materials. *J. Therm. Anal. Calorim.* **2021**, 143 (6), 3923−3934.

(18) Cong, L.; Zou, B.; Palacios, A.; Navarro, M. E.; Qiao, G.; Ding, Y. Thickening and gelling agents for formulation of thermal energy storage materials − A critical review. *Renewable Sustainable Energy Rev.* **2022**, 155, 111906.

(19) Tiemei, L.; Zixuan, Z.; Hu, H.; Rui, Y. Sodium Polyacrylate/ Sodium Sulfate Decahydrate Phase Change Composites. *J. Funct. Polym.* **2020**, 33 (2), 157−164.

(20) Cabeza, L. F.; Svensson, G.; Hiebler, S.; Mehling, H. Thermal performance of sodium acetate trihydrate thickened with different materials as phase change energy storage material. *Appl. Therm. Eng.* **2003**, 23 (13), 1697−1704.

(21) Fang, M.; Zhang, X.; Ji, J.; Hua, W.; Zhao, Y.; Liang, J. Optimal selection of thickeners for the phase change material of $Na2S2O3 \cdot 5H2O$−$CH3COONa \cdot 3H2O$. *J. Therm. Anal. Calorim.* **2021**, 147 (15), 8177−8188.

(22) Oh, K.; Kwon, S.; Xu, W.; Wang, X.; Toivakka, M. Effect of micro- and nanofibrillated cellulose on the phase stability of sodium sulfate decahydrate based phase change material. *Cellulose* **2020**, 27 (9), 5003−5016.

(23) Liu, Y.; Yu, K.; Gao, X.; Ren, M.; Jia, M.; Yang, Y. Enhanced thermal properties of hydrate salt/poly (acrylate sodium) copolymer hydrogel as form-stable phase change material via incorporation of hydroxyl carbon nanotubes. *Sol. Energy Mater. Sol. Cells* **2020**, 208, 110387.

(24) Li, G.; Zhang, B.; Li, X.; Zhou, Y.; Sun, Q.; Yun, Q. The preparation, characterization and modification of a new phase change material: $CaCl2 \cdot 6H2O$−$MgCl2 \cdot 6H2O$ eutectic hydrate salt. *Sol. Energy Mater. Sol. Cells* **2014**, 126, 51−55.

(25) Akamo, D. O.; Li, K.; Turnaoglu, T.; Kumar, N.; Li, Y.; Pekol, C.; Bibhanshu, N.; Goswami, M.; Hirschey, J.; LaClair, T. J.; et al. Enhanced thermal reliability and performance of calcium chloride hexahydrate phase change material using cellulose nanofibril and graphene nanoplatelet. *J. Energy Storage* **2024**, 75, 109560.

(26) Riahinezhad, M.; Kazemi, N.; McManus, N.; Penlidis, A. Effect of ionic strength on the reactivity ratios of acrylamide/acrylic acid (sodium acrylate) copolymerization. *J. Appl. Polym. Sci.* **2014**, 131 (20), 40949.

(27) Milián, Y. E.; Gutiérrez, A.; Grágeda, M.; Ushak, S. A review on encapsulation techniques for inorganic phase change materials and the influence on their thermophysical properties. *Renewable Sustainable Energy Rev.* **2017**, 73, 983−999.

(28) Nazir, H.; Batool, M.; Bolivar Osorio, F. J.; Isaza-Ruiz, M.; Xu, X.; Vignarooban, K.; Phelan, P.; Inamuddin; Kannan, A. M. Recent developments in phase change materials for energy storage applications: A review. *Int. J. Heat Mass Transfer* **2019**, 129, 491−523.

(29) Li, Y.; Kumar, N.; Hirschey, J.; Akamo, D. O.; Li, K.; Tugba, T.; Goswami, M.; Orlando, R.; LaClair, T. J.; Graham, S.; et al. Stable salt hydrate-based thermal energy storage materials. *Composites, Part B* **2022**, 233, 109621.

(30) Goswami, M.; Kumar, N.; Li, Y.; Hirschey, J.; LaClair, T. J.; Akamo, D. O.; Sultan, S.; Rios, O.; Gluesenkamp, K. R.; Graham, S. Understanding supercooling mechanism in sodium sulfate decahydrate phase-change material. *J. Appl. Phys.* **2021**, 129 (24), 245109.

(31) Sankar Deepa, A.; Tewari, A. Phase transition behaviour of hydrated Glauber's salt based phase change materials and the effect of ionic salt additives: A molecular dynamics study. *Comput. Mater. Sci.* **2022**, 203, 111112.

(32) Neuefeind, J.; Feygenson, M.; Carruth, J.; Hoffmann, R.; Chipley, K. K. The Nanoscale Ordered MAterials Diffractometer NOMAD at the Spallation Neutron Source SNS. *Nucl. Instrum. Methods Phys. Res., Sect. B* **2012**, 287, 68−75.

(33) Mcnutt, N. W.; Rios, O.; Feygenson, M.; Proffen, T. E.; Keffer, D. J. Structural analysis of lignin-derived carbon composite anodes. *J. Appl. Crystallogr.* **2014**, 47, 1577−1584.

(34) Tucker, M. G.; Keen, D. A.; Dove, M. T.; Goodwin, A. L.; Hui, Q. RMCProfile: Reverse Monte Carlo for polycrystalline materials. *J. Phys.: Condens. Matter* **2007**, 19 (33), 335218.

(35) Plimpton, S. Fast Parallel Algorithms for Short-Range Molecular Dynamics. *J. Comput. Phys.* **1995**, 117, 1−19.

(36) Yu, M.; Every, H. A.; Jiskoot, W.; Witkamp, G. J.; Buijs, W. Molecular structure of dextran sulphate sodium in aqueous environment. *J. Mol. Struct.* **2018**, 1156, 320−329.

(37) Hanwell, M. D.; Curtis, D. E.; Lonie, D. C.; Vandermeersch, T.; Zurek, E.; Hutchison, G. R. Avogadro: an advanced semantic chemical editor, visualization, and analysis platform. *J. Cheminf.* **2012**, 4 (1), 17.

(38) Kamburov, S.; Schmidt, H.; Voigt, W.; Balarew, C. Similarities and peculiarities between the crystal structures of the hydrates of sodium sulfate and selenate. *Acta Crystallogr., Sect. B: Struct. Sci., Cryst. Eng. Mater.* **2014**, 70 (4), 714−722.

(39) Mayo, S. L.; Olafson, B. D.; Goddard, W. A. G. DREIDING: A Generic Force Field for Molecular Simulations. *J. Phys. Chem.* **1990**, 94, 8897−8909.

(40) Schmid, N.; Eichenberger, A. P.; Choutko, A.; Riniker, S.; Winger, M.; Mark, A. E.; van Gunsteren, W. F. Definition and testing of the GROMOS force-field versions 54A7 and 54B7. *Eur. Biophys. J.* **2011**, 40 (7), 843−856.

(41) Berendsen, H. J. C.; Grigera, J. R.; Straatsma, T. P. The missing term in effective pair potentials. *J. Phys. Chem.* **1987**, 91, 6269−6271.

(42) Hoover, W. G. Canonical dynamics: Equilibrium phase-space distributions. *Phys. Rev. A* **1985**, 31, 1695−1697.

(43) Nosé, S. A molecular dynamics method for simulations in the canonical ensemble. *Mol. Phys.* **2002**, 100 (1), 191−198.

(44) Akamo, D. O.; Ijaola, A. O.; George, T. T.; Page, K.; Keffer, D. J.; Li, Y.; Goswami, M.; LaClair, T. J.; Gluesenkamp, K.; Rios, O. Bibliometric review and recent advances in total scattering pair distribution function analysis : 21 years in retrospect. *Eur. J. Mater.* **2022**, 3 (1), 2150897.

(45) Christiansen, T. L.; Cooper, S. R.; Jensen, K. M. Ø. There's no place like real-space: elucidating size-dependent atomic structure of nanomaterials using pair distribution function analysis. *Nanoscale Adv.* **2020**, 2, 2234−2254.

(46) Billinge, S. J. L. The rise of the X-ray atomic pair distribution function method: a series of fortunate events. *Philos. Trans. R. Soc., A* **2019**, 377 (2147), 20180413.

(47) Wang, X.; Tan, S.; Yang, X.-Q.; Hu, E. Pair distribution function analysis: Fundamentals and application to battery materials. *Chin. Phys. B* **2020**, *29* (2), 028802.

(48) Cui, S.; Liu, J.; Selvan, M. E.; Keffer, D. J.; Edwards, B. J.; Steele, W. V. A Molecular Dynamics Study of a Nafion Polyelectrolyte Membrane and the Aqueous Phase Structure for Proton Transport. *J. Phys. Chem. B* **2007**, *111*, 2208−2218.

(49) Jang, S. S.; Lin, S. T.; Maiti, P. K.; Blanco, M.; Goddard, W. A.; Shuler, P.; Tang, Y. Molecular dynamics study of a surfactant-mediated decane-water interface: Effect of molecular architecture of alkyl benzene sulfonate. *J. Phys. Chem. B* **2004**, *108* (32), 12130−12140.

(50) Rao, Z.; Wang, S.; Peng, F. Self diffusion and heat capacity of n-alkanes based phase change materials: A molecular dynamics study. *Int. J. Heat Mass Transfer* **2013**, *64*, 581−589.

(51) Sun, M.; Liu, T.; Li, M.; Liu, T.; Wang, X.; Chen, G.; Jiang, D. Experimental and molecular dynamic simulation of supercooling phenomenon of sodium acetate trihydrate. *J. Energy Storage* **2023**, *62*, 106956.